Mechanism and Machine Theory 225 (2026) 106454

Contents lists available at ScienceDirect

Mechanism and Machine Theory

journal homepage: www.elsevier.com/locate/mechmt

Research paper

Uncontrolled collision dynamics and the role of dual motor actuators in impact mitigation

Amin Khorasani[a,b,1,*], Thierry Hubert[a,c], Nathan Desmedt[a,d], Raphaël Furnémont[a,c], Alexandre Girard[e], Bram Vanderborght[a,b], Tom Verstraten[a,b]

[a] Brubotics, Vrije Universiteit Brussel, Brussels, Belgium
[b] Imec, Leuven, Belgium
[c] Flanders Make, Belgium
[d] Fellow of the Research Foundation, Flanders (FWO), Belgium
[e] Department of Mechanical Engineering, Université de Sherbrooke, QC, Canada

ARTICLE INFO

Keywords:
Dual motor actuator
Collision in robotics
Impact mitigation
Safe interaction
Redundant actuation

ABSTRACT

Human-robot interaction involves unavoidable collision risks, especially in uncontrolled impacts where forces rise rapidly. Conventional single-drive actuators (SDAs) exhibit high reflected inertia, limiting their intrinsic safety and motivating actuator designs that can passively reduce impact severity. This paper investigates Dual Motor Actuators (DMAs) as a promising solution for passive impact mitigation. We develop a high-fidelity collision model and a complementary analytical formulation that together capture the dynamics of robot-human collisions, including the influence of actuator inertia distribution. The models are validated through simulations and experiments using high-frequency force measurements at 2 kHz. Experimental and simulation results show that DMAs can passively reduce peak impact forces by up to 34% compared to SDAs, despite identical output torque capability. The analytical model accurately predicts peak forces and time-to-peak across a wide range of conditions, showing that collisions reach their maximum force within 17–79 ms. This narrow response window aligns with the experimentally observed 9 ms detection latency at a 1 kHz sampling rate, underscoring the importance of intrinsic mechanical safety. Together, these results demonstrate that DMAs offer a robust actuator architecture for passive impact mitigation and provide actionable design insights for safer collaborative and humanoid robots.

1. Introduction

Unintended and uncontrolled collisions remain one of the critical safety challenges in collaborative and humanoid robotics. In such events, no controller can react quickly enough to influence the initial impact, making the robot's intrinsic mechanical properties; its reflected inertia, damping, and passive energy distribution, the sole determinants of collision severity. This paper investigates whether Dual Motor Actuators (DMAs), with their ability to redistribute internal kinetic energy and shape reflected inertia, can intrinsically

* Corresponding author.
E-mail address: amin.khorasani@vub.be (A. Khorasani).
[1] This research is supported by Research Foundation Flanders, Belgium (FWO) SBO project ELYSA Project (grant number S001821N) and FWO fellowship grant 1SA6A26N.

https://doi.org/10.1016/j.mechmachtheory.2026.106454
Received 11 December 2025; Received in revised form 19 February 2026; Accepted 13 April 2026
Available online 25 April 2026

mitigate impact forces during these fast, passive collision events. We show that this capability leads to substantially lower peak forces than conventional Single Drive Actuators (SDAs), even without any control intervention.

Unlike traditional industrial robots, which operate in isolated environments, cobots must safely interact with humans in shared workspaces. This demands actuator and structural designs that inherently mitigate the risk of injury during unintended collisions [1]. While external perception systems [2] and reactive control strategies can avoid some collisions, their latency and reliance on sensing pipelines limit effectiveness in fast or unpredictable contact scenarios [3,4].

To improve intrinsic safety, many studies have focused on reducing the mechanical impedance of robots, especially through compliant actuators and optimized lightweight and compliant links structures [5,6]. One widely adopted strategy in actuator level is Series Elastic Actuator (SEA), which introduces mechanical compliance between the motor and the load. SEAs decouple the actuator's inertia and enable better force control [7,8], but they also suffer from reduced control bandwidth and added design complexity, which can hinder performance in high-precision tasks [9].

Soft robotic links and viscoelastic padding have also been employed to passively absorb collision energy [10,11]. While beneficial, excessive compliance reduces stiffness and positional accuracy, impacting performance in applications requiring fast and precise motion. Furthermore, the damping properties required to substantially attenuate collision forces, especially at typical robot speeds, remain an open research question [12].

Another effective method for mitigating collision forces is by reducing the actuator's reflected impedance, which encompasses not only reflected inertia but also the stiffness and damping perceived at the output, influenced by both the actuator's internal dynamics and its transmission efficiency. Lowering this overall impedance helps reduce the peak forces transmitted during an impact. Various approaches have been proposed to achieve this, such as using compact, low-inertia actuators [13], highly efficient and backdrivable transmissions like modified Wolfrom-based gearboxes [14], or clutched actuators that mechanically decouple the motor and gearbox from the load during a collision [15]. However, the latter approach often involves complex mechanical integration and contributes additional mass to the robot joints, negatively affecting the system's responsiveness and efficiency.

Recent developments have introduced Dual Motor Actuators (DMAs) [16–18] and Differential Elastic Actuators (DEAs) [19–21], which offer more versatile impedance control and inertia shaping, which enable dynamic tuning of output impedance and reflected inertia for improved safety and control performance. In DMAs, two motors are connected via differential or hybrid transmission systems with distinct gear ratios. This architecture allows the joint output speed to be synthesized through various combinations of internal motor speeds, enabling real-time manipulation of kinetic energy distribution [22,23]. This, in turn, enables dynamic modulation of the actuator's reflected inertia, a property that is typically fixed in single-drive actuators. By actively shaping the reflected inertia, DMAs provide a unique opportunity to enhance safety during collisions by minimizing the kinetic energy at the output, making them particularly effective in mitigating impact forces [24].

Despite these promising results, most prior work focuses on controlled or task-driven scenarios, often neglecting the actuator's behavior during unintended, purely passive collisions, where at impact events no control loop can react fast enough to alter the initial response, and the outcome depends only on the intrinsic mechanical properties of the actuator and robot structure. This paper investigates whether the unique capability of DMAs to redistribute internal energy and dynamically reduce reflected inertia can provide tangible safety benefits during such uncontrolled collisions. We validate this hypothesis through analytical modeling, high-fidelity simulation, and experimental evaluation using a certified measurement system. We then simulate and experimentally compare the collision responses of Single Drive Actuators (SDAs) with different inertias and gear ratios to those of DMA configurations.

These insights provide actionable design guidelines for designers seeking to optimize both safety and performance in future cobot and humanoid systems.

The remainder of the paper is structured as follows. Section 2 introduces the DMA and presents the collision modeling approach, supported by experimental data from falling-object impact tests on compliant surfaces. It also analyzes how soft bodies and appropriate damping properties can contribute to achieving reduced and better-mitigated collision forces. Section 3 studies a single drive actuator collision scenario through simulation and analyzes the potential of the DMA to achieve lower reflected inertia compared to single-drive actuators, and how this influences collision mitigation even in an uncontrolled scenario. Section 4 presents the experimental validation of collision responses using both actuator types, and Section 5 concludes the paper.

2. Actuator influence and collision modeling for impact safety

Before introducing the collision dynamics model used in this work, we first discuss the Dual Motor Actuator (DMA) and highlight its potential to passively reduce collision severity by dynamically altering its reflected inertia. Understanding this capability is essential for motivating the subsequent modeling framework. After this brief overview, the section presents a dynamic collision model that captures the coupled robot-human interaction using a lumped mass-spring-damper representation.

2.1. Dual motor actuator architecture, kinematics, and its dynamics

The DMA is a kinematically redundant actuator architecture composed of two motors (sun and ring), a differential, and an auxiliary gearbox. Unlike traditional single-drive actuators, the DMA allows multiple combinations of internal motors speed to achieve the same joint output motion. This redundancy enables dynamic redistribution of internal kinetic energy, which significantly affects the actuator's reflected inertia and, consequently, its behavior during collisions.

Fig. 1 illustrates the DMA architecture: the two motors (a sun motor and a ring motor) are coupled via a planetary differential and connected to the output through an additional gearbox. The sun motor and the ring motor each contribute to the output motion

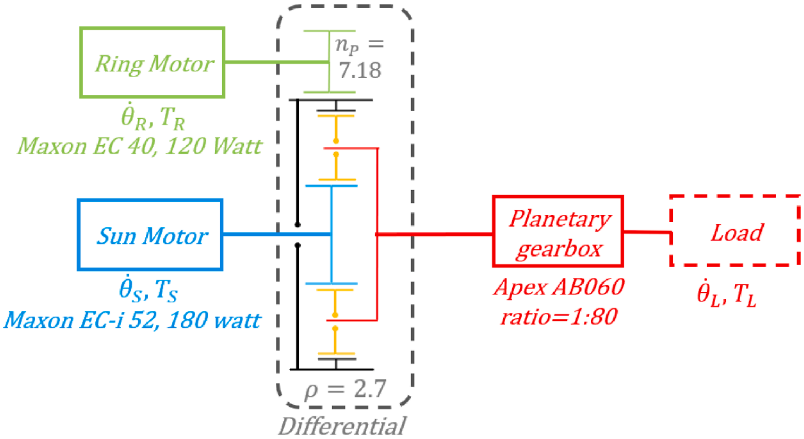

Fig. 1. DMA Schematic, consisting of two motors (Sun and Ring drive train) as the inputs and represented $\dot{\theta}_L$ as the output speed.

through their respective gear paths, characterized by gear ratios ρ (differential ring to sun gear ratio), n_P (ratio of the additional pair of gears in the ring gear) and n_G (ratio of the auxiliary gearbox). The differential allows these motors to operate independently or in a coordinated fashion, providing flexibility in how their speeds ($\dot{\theta}_S, \dot{\theta}_R$) combine to produce the output speed $\dot{\theta}_L$.

This design enables the DMA to dynamically modulate its kinetic energy in real time by adjusting the internal speed ratio [17,25], and overall it has lower kinetic energy and hence lower reflected inertia in comparison to a single drive actuator, as discussed in [24]. As shown in the literature, such redundancy can improve force control and compliance, and is particularly advantageous for safety-critical human-robot interaction. In this work, we investigate how this unique capability influences the collision dynamics when the DMA is subjected to an unexpected impact, focusing on its potential to passively mitigate peak impact forces even without active control, which is studied in [24].

The relationship between the motor speeds and the output velocity is given by:

$$\dot{\theta}_L = R_S\dot{\theta}_S + R_R\dot{\theta}_R, \tag{1}$$

where $\dot{\theta}_L$ is output speed, $\dot{\theta}_S$ and $\dot{\theta}_R$ are the angular velocities of the sun and ring drive trains, respectively, and R_S, R_R are their inverse gear reduction ratios.

General forward dynamic model of the DMA is governed by Newton-Euler dynamics at the motor side, with the resulting torques expressed as:

$$\begin{bmatrix} T_{mS} \\ T_{mR} \end{bmatrix} = M \begin{bmatrix} \ddot{\theta}_S \\ \ddot{\theta}_R \end{bmatrix} + T_v + T_c + R_{SR}T_L, \tag{2}$$

where:

- T_{mS}, T_{mR} are the torques generated by the sun and ring motors,
- $\ddot{\theta}_S, \ddot{\theta}_R$ are their angular accelerations,
- M is the mass matrix, defined as:

  $$M = \begin{bmatrix} J_S + R_S^2 J_o & R_S R_R J_o \\ R_S R_R J_o & J_R + R_R^2 J_o \end{bmatrix},$$

  with $J_o = J_C + J_L$, as J_C is carrier inertia and J_L is load inertia.
- $R_{SR} = \begin{bmatrix} R_S \\ R_R \end{bmatrix}$ couples the load-side torque to each motor.
- $T_v = \begin{bmatrix} v_S\dot{\theta}_S \\ v_R\dot{\theta}_R \end{bmatrix}$ is the viscous friction torque at each motor side,
- $T_c = \begin{bmatrix} \text{sign}(\dot{\theta}_S)T_{cS} \\ \text{sign}(\dot{\theta}_R)T_{cR} \end{bmatrix}$ is the Coulomb friction torque at motors side,
- $T_L = (F_{env} - M_{pl}g)l$ is the load torque from an external collision or the force of the environment F_{env}, and the gravitational effect ($M_{pl}g$) affecting with length of the link l in the case of a collision in line with gravity.

2.2. Kinetic energy of the DMA

The mass matrix M not only governs the forward dynamics of the DMA but also fully determines its kinetic energy, since it captures how the sun and ring drive trains interact through the differential. Using the generalized motor-side velocity vector

$$\dot{q} = \begin{bmatrix} \dot{\theta}_S \\ \dot{\theta}_R \end{bmatrix},$$

the total kinetic energy of the actuator can be expressed compactly as

$$T = \frac{1}{2}\dot{q}^T M \dot{q}. \tag{3}$$

Expanding this quadratic form yields

$$T = \frac{1}{2}\Big[\big(J_S + R_S^2 J_o\big)\dot{\theta}_S^2 + 2R_S R_R J_o \dot{\theta}_S \dot{\theta}_R + \big(J_R + R_R^2 J_o\big)\dot{\theta}_R^2\Big]. \tag{4}$$

A key implication of Eq. (4) is that, although the load-side speed $\dot{\theta}_L$ is unique, the two internal motor speeds introduce an additional degree of freedom in how kinetic energy is distributed inside the actuator. To compactly describe this distribution for a given output speed, we write the kinetic energy as

$$T = \tfrac{1}{2} J_{\text{DMA,eq}}(\gamma)\,\dot{\theta}_L^2, \tag{5}$$

where $J_{\text{DMA,eq}}(\gamma)$ is an energy-equivalent inertia that depends on the internal speed ratio

$$\gamma = \frac{R_R \dot{\theta}_R}{\dot{\theta}_L}. \tag{6}$$

The optimal speed distribution that minimizes this equivalent inertia follows as

$$\gamma_{\text{opt}} = \frac{R_R^2 J_S}{R_R^2 J_S + R_S^2 J_R}. \tag{7}$$

In contrast to conventional single-drive actuators, whose reflected inertia is fixed, a DMA can redistribute its internal kinetic energy between the sun and ring drive trains while maintaining the same output speed. In this work we therefore distinguish between (i) the actuator's impulsive reflected inertia, which is a scalar quantity derived from the mass matrix and used to describe impact behaviour, and (ii) the kinetic energy equivalent inertia $J_{\text{DMA,eq}}(\gamma)$, which we use as a convenient way to parameterize how kinetic energy is shared between the two motors for a given $\dot{\theta}_L$.

Previous work [24] established that, for appropriate choices of γ, the DMA's reflected inertia can be substantially smaller than that of a torque-equivalent single-drive actuator, enabling lower kinetic energy and inherently safer interactions.

As shown through simulation in [24], for our DMA configuration, the kinetic energy remains lower than that of different equivalent SDAs for a certain range of speed distribution γ. This intrinsic variability, arising solely from the actuator's mechanical redundancy, forms the basis for the improved collision response analyzed in the next subsection.

2.3. Physical modeling of collision dynamics

Fig. 2 illustrates a scenario where a human body is pinned between a robotic arm and a rigid structure. A simplified mass spring damper system models the robot as an effective mass m_r and corresponding spring k_r and damper c_r resulting from the mechanical nature of the robot's body, actuation, and control system, approaching a compliant human body. The human is represented by two mechanical elements: a soft silicone damper mimicking skin and subcutaneous fat, and a spring modeling deeper muscles and bones [26]. Although the model is formulated in one dimension along the contact normal, this assumption captures the dominant dynamics of frictionless or ideal normal contact, where the primary force transmission occurs in the normal direction.

The equivalent stiffness on the robot side, k_r, aggregates the combined compliance of the robot links, soft padding, and actuator impedance. This overall stiffness can vary considerably depending on the compliance of transmission components, the robot's configuration, and the stiffness imposed through joint-level control or soft padding. On the other hand, accurate modeling of the human body's mechanical response requires precise knowledge of soft tissue stiffness and damping properties. Ballen-Moreno et al. [27] introduced a method to characterize these properties in vivo, highlighting variability across different body zones by a hyperelastic model considering shear stress and pressure distribution in contact. Research on soft tissue characterization for human-robot safety, however, is still ongoing, with continuing efforts to refine models and capture inter-subject and inter-region variability more accurately. However, in this work on the human side, the total stiffness is modeled as two serial components: The first represents the skin and subcutaneous fat, modeled using silicone dampers with varying stiffness, named as silicone damper stiffness k_d, and various damping properties of c_d. As used in this work's experiments, these silicone layers are characterized by different Shore hardness values related to their material hardness. The second is capturing the stiffness of internal anatomical structures, named as human body stiffness k_h. This modeling approach mirrors the silicone damper and spring configuration used in the certified Pilz Robot Measurement System (PRMS) illustrated in Fig. 4, and employed in this study. The portion of the human body mass m_h involved in compression during a collision depends on the collision area and its geometry, its severity, and the biomechanics of the skin and underlying tissues. For simplicity, the affected mass is approximated as a constant and assumed to be equal to the moving mass collision plate of the PRMS setup used in this study. This value is consistently applied across all simulations and experiments and is detailed in Table 1.

In rigid-link robots lacking joint-level compliance or external soft padding, $k_r \gg k_h$, and the robot behaves as a rigid mass impacting a soft surface [28]. The robot's effective impact mass m_r, often referred to as the reflected mass at the point of contact, plays a pivotal role in determining the severity of collisions. While simplified standards such as ISO-TS 15,066 approximate this quantity as the payload mass plus a fraction of the moving link mass, more advanced formulations offer greater precision by incorporating the

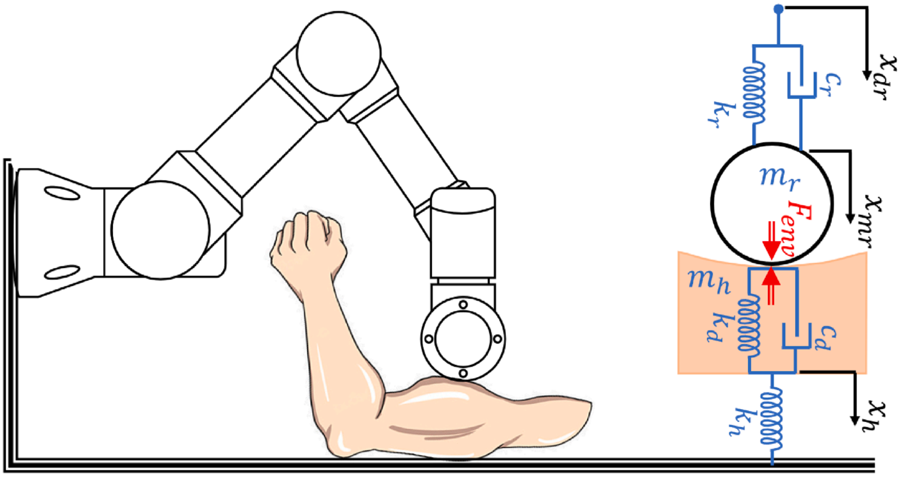

Fig. 2. Schematic representation of a robot colliding with a human body against a rigid surface. The right-hand model abstracts the interaction using a mass-spring-damper system. Here, x_{dr} represents the desired trajectory of the robot's equivalent mass (m_r), x_{mr} is the actual (measured) position of the robot mass, and x_h corresponds to the displacement of the spring modeling human main tissue stiffness, while c_d and k_d are damping and stiffness of the skin and subcutaneous fat.

Table 1
Model and experimental parameters.

Parameter	Symbol	Value
PRMS spring stiffness	k_h	10000–150000 N/m
PRMS moving plate mass with different dampers	m_h	0.42–0.50 kg
PRMS damper stiffness (measured)	k_d	≈330000 N/m
PRMS damping (estimated)	c_d	≈34 N·s/m
Simulation payload mass	M_{pl}	5–20 kg
Experiment setup link length	l	0.34 m
Experiment setup link inertia	J_L	0.087 kg·m^2
Sun (motor + gear) inertia	J_S	1.85×10^{-5} kg·m^2
Sun drive-train Coulomb friction	T_{cS}	0.019 N·m
Sun drive-train viscous friction	v_S	7.5×10^{-5} N·m·s/rad
Ring (motor + pinion) inertia	J_R	9.5×10^{-6} kg·m^2
Ring drive-train Coulomb friction	T_{cR}	0.0058 N·m
Ring drive-train viscous friction	v_R	2.0×10^{-5} N·m·s/rad

robot's full kinematic and inertial properties. Notably, Khatib's framework for operational space dynamics [29] and its application in safety analysis by Hamad et al. [30] and Kirschner et al. [31] provide a rigorous means to compute the directional effective mass as:

$$m_r(\boldsymbol{q}) = \left[\boldsymbol{u}^\top \boldsymbol{\Lambda}_v(\boldsymbol{q})^{-1}\boldsymbol{u}\right]^{-1} \tag{8}$$

Here, $\boldsymbol{u}$ denotes the unit vector in the direction of the collision, and $\boldsymbol{\Lambda}_v(\boldsymbol{q})$ is the translational part of the robot's operational space inertia matrix, which depends on the joint configuration $\boldsymbol{q}$. This formulation captures not only the robot's reflected inertia from actuators and transmissions but also its current pose and the geometry of contact.

2.4. Impact detection and collision behavior

Collision detection in collaborative robots is often based on force/torque thresholds exceeding predefined safety limits. These signals are obtained via joint torque sensors, force and torque sensors at the end effector, inferred from motor currents, or through skin pressure sensing [32]. As illustrated in Fig. 3, noisy signals filtering and control delays affect the force estimation, leading to latency in response performance, so quick identification of collision and its confirmation is required and challenging.

Post-impact, if braking or impedance modulation is triggered, the robot continues to penetrate the surface due to inertia, resulting in peak forces at t_{max} before bouncing back.

2.5. Validation across impact scenarios

In case of an uncontrolled collision, such as a falling free mass m_r represented as the robot's effective mass impacting a human, where the effect of robot damping and stiffness is neglected, the system is modeled as two coupled masses with spring-damper interactions as depicted in Fig. 2. Here, x_{mr} denotes the displacement of the robot's equivalent mass m_r, while x_h represents the

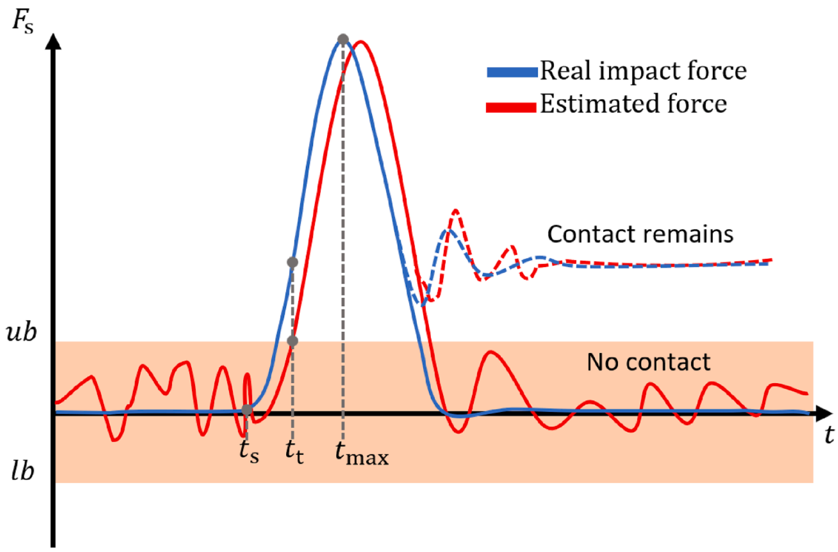

Fig. 3. Collision behavior schematic timeline. Real impact (blue) occurs at t_s, peak force at t_{max}, and filtered environment force estimation (red) crosses the detection bound threshold force (ub or lb) at time t_t. Dashed lines indicate the post-collision force behavior, which may persist due to actuator non-backdrivability, gravity, or residual motor torque, so contact remains in this situation. Negative estimated forces can occur during separation phases or due to modeling inaccuracies and sensor noise. Identifying collision time at t_t is important to know what percentage of peak force has already happened, even before any reaction of the robot controller. (For interpretation of the references to colour in this figure legend, the reader is referred to the web version of this article.)

displacement of the human tissue mass m_h. For simplicity, we assume that the x-axis is oriented along the direction of gravity and that the motion is restricted to one translational degree of freedom (linear impact without rotation or trajectory curvature). Under these assumptions, the interaction force is expressed as:

$$F_{\text{env}} = k_d(x_{mr} - x_h) + c_d(\dot{x}_{mr} - \dot{x}_h) \tag{9}$$

Here, F_{env} is the interaction force between the robot and the contact plate, and k_d and c_d are the stiffness and damping of the soft tissue contact interface, respectively. So at the contact phase ($F_{\text{env}} > 0$) considering restoring force F_s:

$$\ddot{x}_{mr} = \frac{m_r.g - F_{\text{env}}}{m_r} \tag{10}$$

$$\ddot{x}_h = \frac{F_{\text{env}} - F_s}{m_h} \tag{11}$$

Separation phase ($F_{\text{env}} = 0$):

$$\ddot{x}_{mr} = g \tag{12}$$

$$\ddot{x}_h = \frac{-F_s}{m_h} \tag{13}$$

The restoring force F_s is defined as:

$$F_s = k_h x_h \tag{14}$$

In a real collision scenario, such as the one shown in Fig. 4a, the impact does not always consist of a single contact phase. Instead, the colliding body (a steel ball in this case) may separate and re-engage with the compliant surface multiple times, as illustrated in Fig. 4b. These transient separations introduce sub-peaks in the force profile, as the contact is lost and regained throughout the impact event. To realistically capture this behavior, our simulation framework considers separation phases in addition to continuous contact dynamics by switching between different modes based on contact conditions.

With this model in place, we investigate a key question: how long does it take for the peak collision force to occur, and what is its maximum value, under different impact conditions? To answer this, we perform a set of simulations across a wide range of parameters including robot effective mass, human body stiffness, and impact speed. These conditions are selected to reflect realistic safety scenarios in line with ISO/TS 15066, which defines acceptable forces and velocities for robot-human collisions across different body regions.

We consider three principal scenarios:

- Scenario 1: Varying robot mass m_r. Fig. 5a shows the force profiles for robot effective masses m_r ranging from 5 kg (representing a lightweight cobot arm with no payload) to 20 kg (for example, a robot carrying up to a 15 kg payload). The human body stiffness

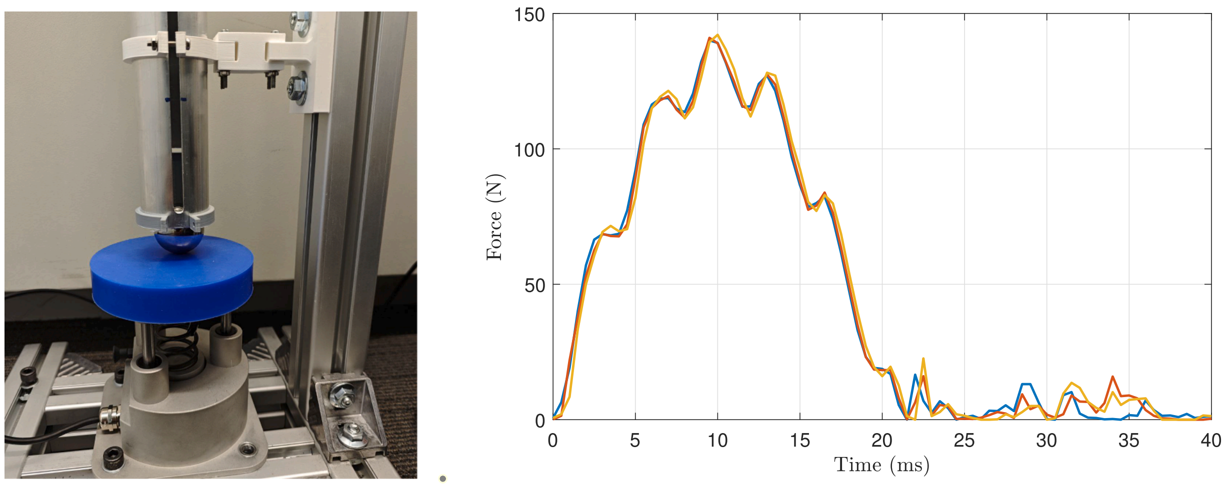

(a) PRMS test setup for ball collision experiments.

(b) Measured force response during repeated ball collisions.

Fig. 4. Experimental setup and results of ball collision with the PRMS device. (a) shows the physical setup used to drop the ball onto the compliant surface. (b) shows the measured collision force (F_s) over time across multiple tests, revealing consistent peak forces and damping behavior. Before reaching the peak forces, there are small local maxima that indicate micro-reengagement of the ball with the sensor plate.

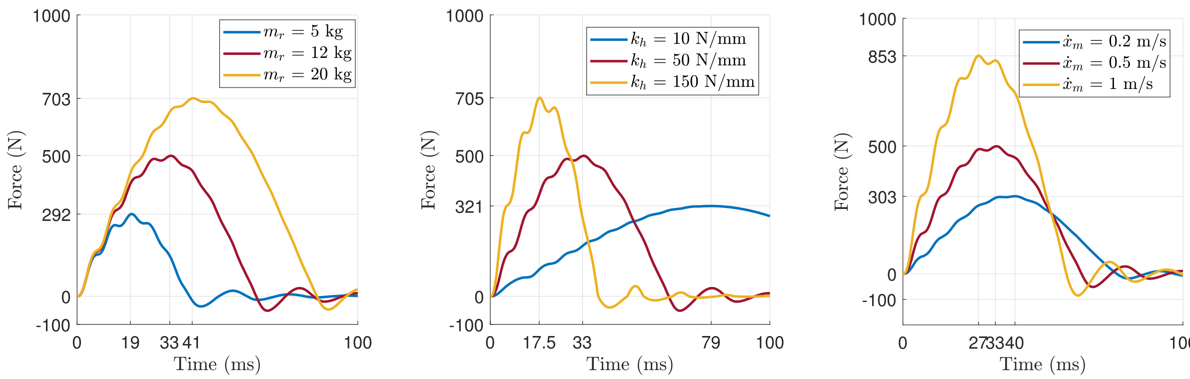

(a) Collision force (F_s) for masses m_r = 5–20 kg at $\dot{x}_{mr}(0) = 0.5$ m/s, medium damping, and stiffness k_h = 50000 N/m. A heavier robot results in a higher peak force and a longer time to reach that peak.

(b) Force profiles (F_s) for human stiffness k_h = 10000–150000 N/m. Peak response time ranges 17–79 ms. Higher body stiffness results in a shorter time to reach peak force.

(c) Force (F_s) variation with impact velocity $\dot{x}_{mr}(0)$ = 0.2–1 m/s. Higher velocity increases peak force and reduces response time. Faster collisions result in higher forces and less time to react.

Fig. 5. Collision force simulations under varying model parameters: robot effective mass, human stiffness, and impact velocity. For each graph, fixed parameters are indicated in (red) in the other graphs. (For interpretation of the references to colour in this figure legend, the reader is referred to the web version of this article.)

is set to $k_h = 50000$ N/m with a medium hardness damper of PRMS setup, closely resembling the PRMS configuration. All impacts occur at an initial speed of $\dot{x}_{mr}(0) = 0.5$ m/s. As a result of these simulations, the time to reach peak force t_{max} varies from 19 ms for a 5 kg robot effective mass to 41 ms, depending on the mass. Peak forces were also recorded as 292 N and 703 N, respectively. A medium robot's effective mass of 12 kg results in a 500 N peak force.

- Scenario 2: Varying human body stiffness k_h. In Fig. 5b, a constant 12 kg robot mass m_r at a fixed speed of $\dot{x}_{mr}(0) = 0.5$ m/s impacts body parts modeled with stiffness ranging from 10000 N/m (e.g., abdomen) to 150000 N/m (e.g., skull). These values are consistent with experimental biomechanical studies. As stiffness increases, peak force occurs faster, ranging from 79 ms for soft tissue to 17 ms for rigid-like structures with the highest stiffness. Peak forces also increase from 321 N to 705 N for the softest spring to the hardest one.
- Scenario 3: Varying impact speed $\dot{x}_{mr}(0)$. Fig. 5c depicts force responses when a medium range $m_r = 12$ kg robot impacts a medium-stiffness human body ($k_h = 50000$ N/m) at different speeds. As expected, higher velocities yield higher peak forces and faster rise times. For instance, a 1 m/s impact reaches its peak in approximately 27 ms and record a peak force of 853 N, while a slower 0.2 m/s collision takes up to 40 ms, and its corresponding peak force is 303 N.

Across these simulated scenarios, our results indicate that the time to reach peak force typically falls within the 17-79 ms range under average conditions. Any control response, including sensor detection, processing, and actuator reaction, must therefore operate within this short window to mitigate impact forces. The importance of system-level design, especially concerning inertia, damping, and compliance, is emphasized in the following sections.

2.6. Analytical estimation of peak force and time to peak

With an assumption of continuous contact during the collision, modeling the interaction as a linear second-order system is possible. In real scenarios, however, the contact may include micro-detachments and secondary impacts, as evidenced in the PRMS measurements discussed earlier in Fig. 4b. These discontinuities affect the smoothness and accuracy of the response but are omitted here for analytical tractability. Therefore, the analysis below provides a simplified yet effective means of estimating peak force based on the dominant dynamic parameters during primary contact.

The system is represented by a mass-spring-damper model with effective mass m_{eff}, effective stiffness k_{eff}, and effective damping coefficient c_{eff} defined at ((20)–(22)), undergoing oscillations in the direction of gravity and governed by the following differential equation:

$$m_{\text{eff}}\,\ddot{x}(t) + c_{\text{eff}}\,\dot{x}(t) + k_{\text{eff}}\,x(t) = m_{\text{eff}}\,g \tag{15}$$

Gravity shifts the static equilibrium position by:

$$x_g = \frac{m_{\text{eff}}\,g}{k_{\text{eff}}} \tag{16}$$

The detailed derivation follows standard second-order system theory and is provided in Appendix A. Here we summarize the main results. For the underdamped case, the time to reach the first peak is obtained as

$$t_{\max} = \frac{-\arctan\left(\frac{\zeta}{\sqrt{1-\zeta^2}}\right) - \phi + k\pi}{\omega_n\sqrt{1-\zeta^2}}, \tag{17}$$

where $\omega_n = \sqrt{k_{\text{eff}}/m_{\text{eff}}}$, $\zeta = c_{\text{eff}}/(2\sqrt{k_{\text{eff}}m_{\text{eff}}})$, and ϕ is set by initial conditions. The corresponding maximum displacement and peak force simplify to

$$x_{\max} = x_g + A\sqrt{1-\zeta^2}\,e^{-\zeta\omega_n t_{\max}}, \tag{18}$$

$$F_{\max} = k_{\text{eff}}\,x_{\max}. \tag{19}$$

This formulation captures the key contributions of mass, stiffness, and damping to peak force response and time to peak force, enabling analytical predictions of impact severity in robotic collisions.

The effective parameters are obtained from the robot-human impact system by combining the robot's moving mass m_r with the mass of the deformable object (e.g., human tissue) m_h, and modeling the tissue compliance and damping as serial elements:

$$m_{\text{eff}} = m_h + m_r, \tag{20}$$

$$k_{\text{eff}} = \frac{k_d\,k_h}{k_d + k_h}, \tag{21}$$

$$c_{\text{eff}} = c_d. \tag{22}$$

To evaluate the accuracy and practical relevance of the proposed simplified analytical model, we compared its predictions against detailed physics-based simulations that explicitly account for contact loss, micro-detachments, and subsequent re-engagement events. Unlike the analytical formulation which assumes continuous contact, the physics-based simulation model captures the transient separation phases that naturally occur during realistic impacts.

In this study, we systematically investigated the influence of each key parameter including effective mass, contact stiffness, and pre-impact velocity individually. This allowed us to examine the model accuracy trends more clearly and to identify specific parameter ranges where deviations may occur.

The comparison for peak force prediction is shown in Fig. 6. Across all parameter sweeps, the mean absolute error (MAE) between the analytical approximation and the physics-based simulation remains below 3.7%, demonstrating that the simplified model provides a close match to the more detailed simulation results even when detachment effects are present, and that it is consistent with the sampled experimental data. The simulations were implemented in MATLAB/Simulink using the Simscape Multibody toolbox, with an ode45 solver running at a fixed step size of 1 ms. Contact dynamics were modeled with a spring-damper formulation that switches modes to capture both compression and separation phases. The results also show that accuracy tends to be highest for higher effective masses and stiffnesses, where the assumption of continuous contact is better satisfied. It should be noted that the experimental validation is constrained by the measurement limits of the PRMS setup, which reliably measures forces up to approximately 500 N. Consequently, experimental tests were conducted within this force range and were limited to the available spring stiffness values and payload masses achievable in our laboratory setup.

Following the same approach, Fig. 7 presents the comparison for the predicted time to reach peak force. The MAE remains below 2.4% across all parameter variations, indicating that the analytical formulation also captures the timing of peak impact forces with high fidelity. As expected, minor deviations occur at lower masses or reduced stiffness, where the effects of detachment and secondary impacts become more pronounced.

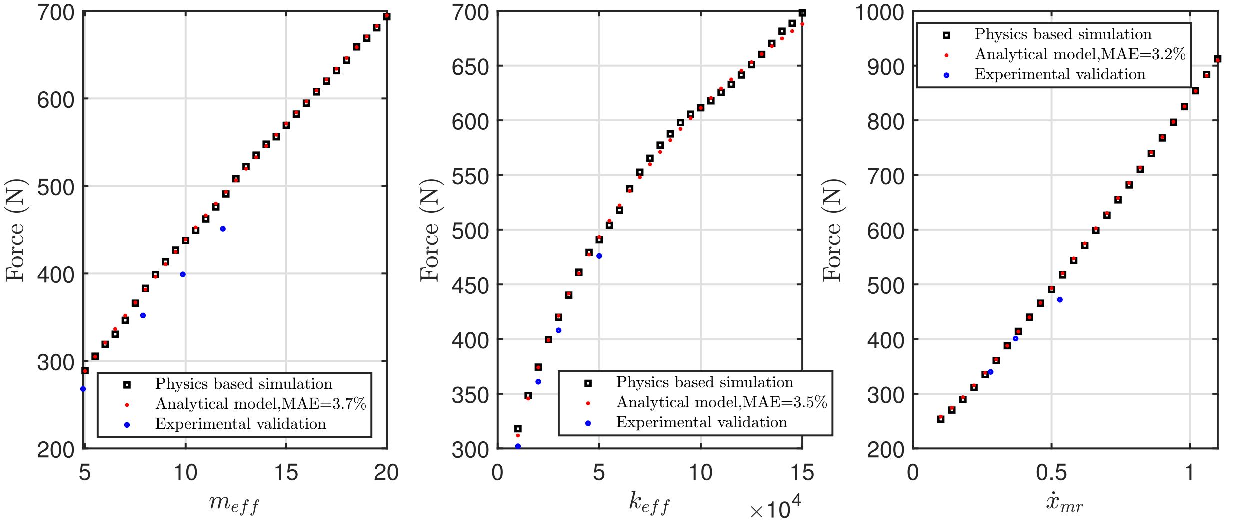

Fig. 6. Comparison of peak collision forces obtained from the physics-based simulation (black squares) , the analytical model (red dots), and experimental validation (blue markers). Results are shown as a function of effective mass m_{eff} (left), effective stiffness k_{eff} (middle), and impact velocity $\dot{x}_{mr}$ (right). The analytical approximation closely matches the physics-based model across all parameter sweeps (MAE 3.2-3.7%), and experimental measurements follow both predictions with the same error range, confirming the validity of the simplified formulation. (For interpretation of the references to colour in this figure legend, the reader is referred to the web version of this article.)

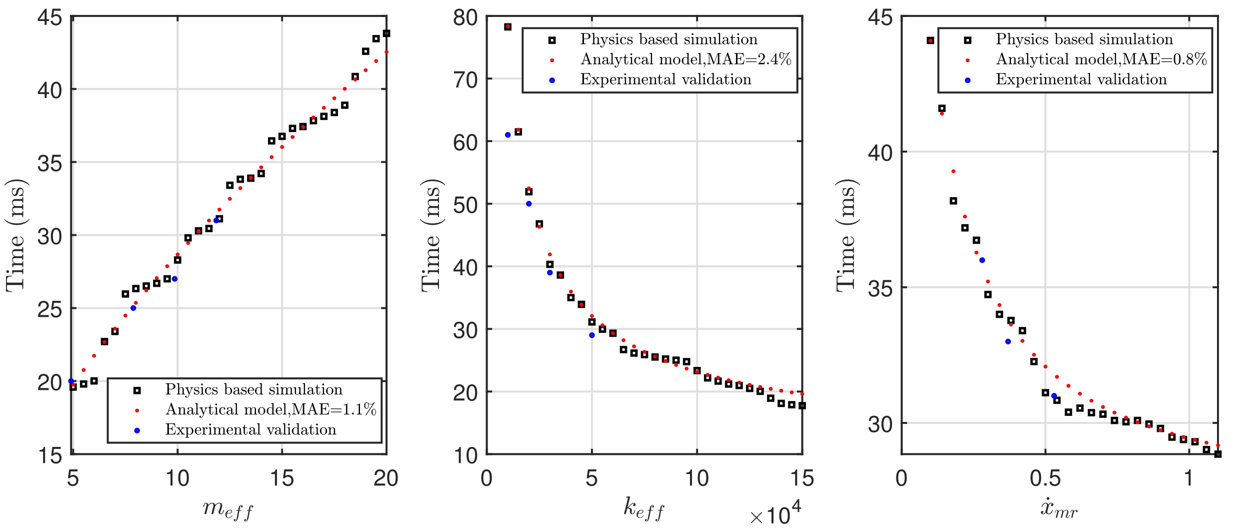

Fig. 7. Time to peak collision force obtained from the physics-based simulation (black squares), the analytical model (red dots), and experimental validation (blue markers). Results are shown as a function of effective mass m_{eff} (left), effective stiffness k_{eff} (middle), and impact velocity $\dot{x}_{mr}$ (right). The analytical approximation closely matches the physics-based model across all parameter variations (MAE $<$2.4%), and experimental results confirm the accuracy of the predicted peak-time behavior. (For interpretation of the references to colour in this figure legend, the reader is referred to the web version of this article.)

Overall, these results confirm that the proposed analytical model is sufficiently accurate for early-stage safety analysis and design optimization, offering a computationally efficient alternative to full physics-based simulations while retaining a high degree of predictive capability.

2.7. Effect of soft padding

While perception systems and intrinsic actuator safety mechanisms are critical, an additional layer of protection can be provided by external soft padding. This form of extrinsic mitigation is often applied to the robot's surface in the form of foam or silicone layers. Although such padding may not prevent injury in every scenario, especially if a human is trapped between the robot payload and a rigid object, it can significantly reduce the severity of collisions when properly designed.

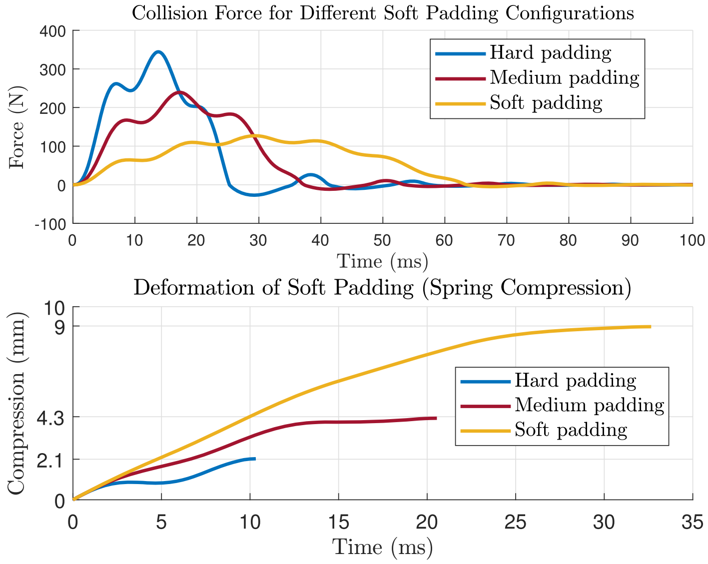

Fig. 8. Effect of soft padding on collision force and deformation. The upper plot shows force profiles for hard, medium, and soft padding during a $\dot{x}_{mr}(0) = 0.5$ m/s impact between a 5 kg robot mass and a human skull. Per ISO/TS 15066, the allowable force for head contact is about 130 N, so only the soft padding (15 N/mm stiffness) reduces the peak force below this limit. The lower plot shows padding deformation, with the softest layer compressing up to 9 mm, effectively absorbing impact energy unlike the stiffer alternatives.

As it can be interpreted in Fig. 2, soft padding can be modeled as a serial spring-damper system connected to the human body's elastic response. The effective stiffness $k_{\mathrm{d,eff}}$ and effective damping $c_{\mathrm{d,eff}}$ of system are then given by the serial combination of the robot-side padding and the human-side body properties. These are formulated as:

$$k_{\mathrm{d,eff}} = \left(\frac{1}{k_{\mathrm{eff}}} + \frac{1}{k_r}\right)^{-1}, \quad c_{\mathrm{d,eff}} = \left(\frac{1}{c_d} + \frac{1}{c_r}\right)^{-1} \tag{23}$$

Here, k_r and c_r denote the stiffness and damping characteristics of the padding layer, while k_{eff} and c_d represent those of the human skin and tissue parameters, as previously defined.

To investigate the impact of padding characteristics on collision safety, we simulate an uncontrolled collision where a $m_r = 5$ kg effective robot mass impacts a rigid skull-like human structure at $\dot{x}_{mr}(0) = 0.5$ m/s. Three padding configurations are considered attached to the robot, from Hard padding ($k_p = 100$ N/mm), and Medium padding ($k_p = 60$ N/mm) to Soft padding ($k_p = 15$ N/mm). For all of these padding layers, the damping parameter of the human is similar to that used in the PRMS setup. Fig. 8 presents the force profiles and corresponding padding compression (deformation) for each case. As shown, only the softest padding successfully reduces the peak collision force below the 130 N threshold defined by ISO/TS 15066 for head impacts, for example.

However, it is important to note that the padding must maintain a stable (approximately linear) stiffness and damping response throughout its full compression range, especially under high-speed collisions, which is not realistic. For instance, in the tested scenario, a 5 kg effective mass colliding at $\dot{x}_{mr}(0) = 0.5$ m/s, the soft padding needs to compress around 9 mm within a short impact duration of less than 32 ms to achieve sufficient force mitigation. If the material exhibits stiffening behavior during compression (i.e., its stiffness increases as it deforms), the contact force will rise more quickly than expected, diminishing its protective effect. This means that although the initial stiffness may be low, the benefit is lost if the padding hardens too soon during compression. In such cases, to maintain effective impact mitigation, either a thicker layer of padding or a material with a lower initial stiffness is required to compensate for the stiffening effect and keep the peak forces within acceptable safety limits.

In summary, soft padding can substantially reduce impact forces during human-robot collisions, especially when targeting sensitive regions like the head. These results demonstrate that careful selection of material stiffness and damping can achieve compliance with ISO safety thresholds. While this study focuses primarily on the variation of stiffness and damping properties across padding materials, it is important to acknowledge that padding thickness is another critical parameter affecting energy absorption and deformation characteristics. In our simulations, the softest padding configuration was modeled with sufficient thickness to permit up to 9 mm of linear compression without material saturation or stiffening. However, achieving such levels of compliance in practice often requires substantially thicker padding, which may not be feasible for many robotic applications due to constraints on size, added mass, and design integration. More importantly, it is generally not possible to cover all moving components with soft padding, particularly the payloads in many industrial and service applications; so the protective effect remains limited to selected areas.

In the next section, we explore how the robot's actuator design and reflected inertia can further influence collision behavior.

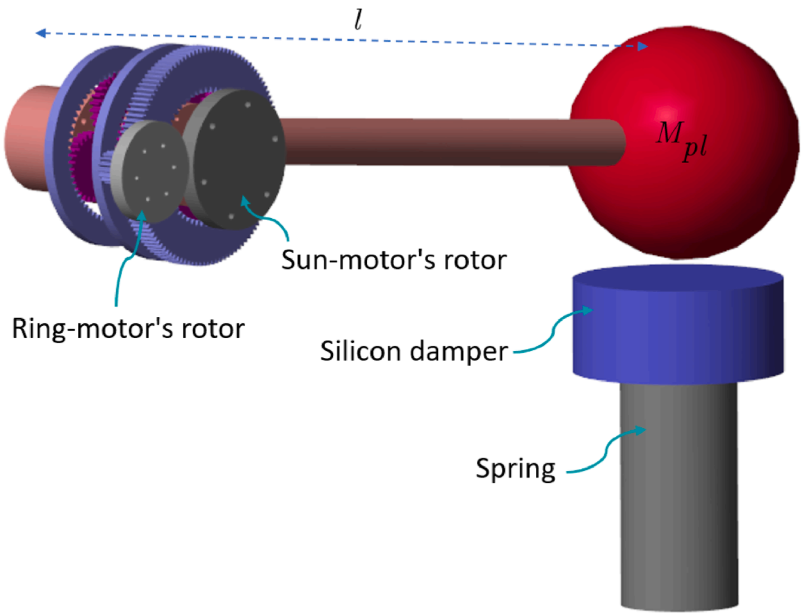

Fig. 9. Schematic of actuator and collision measurement setup modeled in simscape multibody Matlab.

3. Actuator influence in collision

At the previous section we analyzed the collision between a falling effective mass and a compliant human body, showing how the mass's kinetic energy is transferred into deformation and absorbed by the human-side viscoelastic elements. In a real robot, however, the situation is more complex: the kinetic energy at impact does not originate solely from the payload or link inertia, but also from the actuator and transmission dynamics. The reflected inertia of the motor and gearbox can substantially increase the system's effective mass at the contact point, thereby intensifying collision severity. To understand this contribution, we first investigate the collision behavior of a Single Drive Actuator (SDA), where the reflected inertia is fixed by the motor-gearbox configuration. We then extend this analysis to a DMA, which can redistribute internal kinetic energy and dynamically modulate its reflected inertia, offering the potential for intrinsically safer collision responses.

3.1. Collision dynamics with SDA

We first simulate the collision dynamics of a robotic system actuated by an SDA. The actuator consists of a single motor and gearbox, modeled through its reflected inertia at the collision point. We analyze two motor configurations with different inertias and gear ratios, corresponding to the motors we will later use in a DMA.

The overall system is modeled as a coupled mass-spring-damper system, where a payload mass M_{pl}, attached to a robot link with length l and inertia J_{L}, and an actuator with reflected inertia J_{ref} impacts a deformable object with mass m_h, spring stiffness k_h, and damping coefficient c_d. A schematic of this actuator is depicted in Fig. 9 for DMA, while in SDA configuration, only the sun motor or the ring motor is active.

For the SDA, a single motor with inertia J_{act} is connected to the joint through a gearbox with ratio N, resulting in a reflected inertia

$$J_{\mathrm{ref}} = N^2 J_{\mathrm{act}}. \tag{24}$$

Together with the link inertia J_L and payload mass M_{pl}, the robot's effective mass at the contact point is

$$m_r^{\mathrm{SDA}} = M_{\mathrm{pl}} + \frac{J_L + J_{\mathrm{ref}}}{l^2}, \tag{25}$$

where l is the link length. This expression highlights the trade-off between motor inertia and gear ratio: increasing N amplifies torque but also increases the perceived inertia during impact.

Coupling m_r^{SDA} with the human-side deformable mass m_h and the viscoelastic elements (k_d, k_h, c_d) from Eqs. (9)–(13) yields the scalar collision model

$$m_{\mathrm{eff}}^{\mathrm{SDA}}\ddot{x}(t) + c_{\mathrm{eff}}\dot{x}(t) + k_{\mathrm{eff}}x(t) = m_{\mathrm{eff}}^{\mathrm{SDA}}g, \tag{26}$$

with $m_{\mathrm{eff}}^{\mathrm{SDA}} = m_r^{\mathrm{SDA}} + m_h$. The closed-form peak-force expressions in Appendix A apply directly by substituting $m_{\mathrm{eff}} = m_{\mathrm{eff}}^{\mathrm{SDA}}$.

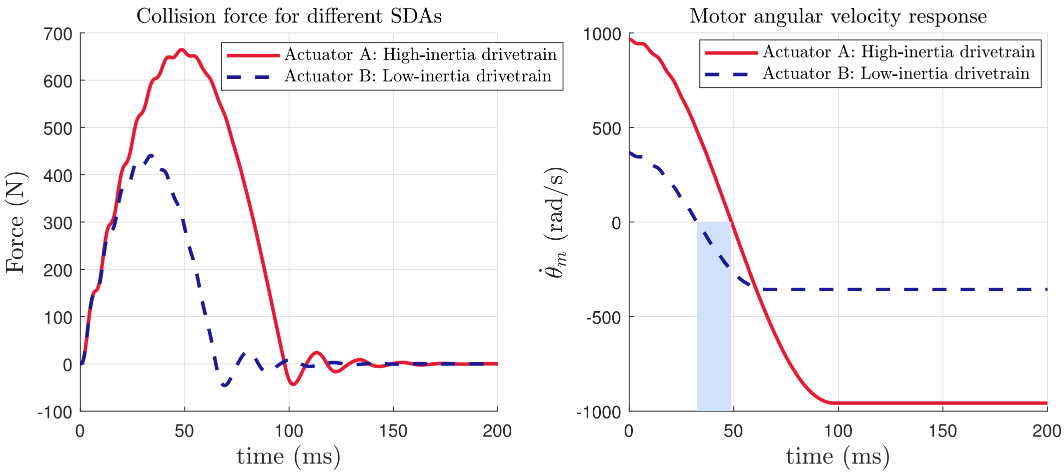

Fig. 10. Left: Collision force and motor angular velocity for two SDA configurations. Actuator A, shown with a solid red line, reaches a peak force of 665 N. Although it has a lower gear reduction, it exhibits higher inertia. Actuator B, shown with a dashed blue line, reaches a peak force of 402 N and has lower reflected inertia. Right: Motor angular velocity response. The shaded interval (33-49 ms) marks the time required for the motor to decelerate to zero speed (stop) after impact initiation. The high inertia configuration (Actuator A) requires a longer stopping time, whereas the low inertia configuration (Actuator B) stops sooner. (For interpretation of the references to colour in this figure legend, the reader is referred to the web version of this article.)

3.1.1. *Motor configurations and reflected inertia*

Two actuator configurations have been considered:

- Actuator A: with $J_{\text{act}} = 85\ \text{g} \cdot \text{cm}^2$, gear ratio $N = 688$
- Actuator B: with $J_{\text{act}} = 180\ \text{g} \cdot \text{cm}^2$, gear ratio $N = 297$

In this case, Actuator A is equipped with a high-speed motor and lower torque, requiring a higher gear ratio to deliver the same torque. In contrast, Actuator B uses a high-torque motor with a lower gear reduction.

Although both actuators are capable of delivering the required torque independently, they exhibit different dynamic behaviors due to their reflected inertias.

3.1.2. *Results and observations*

Fig. 10 shows the collision force and motor angular velocity response for both configurations. The low-inertia motor (Actuator A), with a higher gear ratio, leads to a significantly higher reflected inertia at the point of contact. As a result, it induces a peak force of approximately 665 N during impact. On the other hand, Actuator B, despite its higher rotor inertia, benefits from a lower gear ratio, resulting in reduced reflected inertia and a lower peak collision force of approximately 402 N.

This result highlights the inherent trade-off between motor inertia and gear ratio in designing safe and responsive actuators. While Actuator A provides torque amplification through a high gear ratio, it amplifies the reflected inertia and thus increases collision forces. In contrast, Actuator B reduces reflected inertia by sacrificing gear amplification. These insights form the foundation for introducing a DMA, where both motors are used together to distribute kinetic energy and reduce impact forces more effectively. The DMA approach is explored in the next subsection.

3.2. *Collision dynamics with a DMA*

To evaluate the DMA's passive impact behavior, we assume that both motors are unactuated during collision,

$$T_{mS} = 0, \qquad T_{mR} = 0,$$

so that the system evolves solely under the external contact force and the internal viscous and Coulomb friction terms. The forward dynamics at the motor side are given by

$$\begin{bmatrix} T_{mS} \\ T_{mR} \end{bmatrix} = M \begin{bmatrix} \ddot{\theta}_S \\ \ddot{\theta}_R \end{bmatrix} + T_v + T_c + R_{SR} T_L, \tag{27}$$

with M the motor-side mass matrix, R_{SR} the load-to-motor coupling ratio.

In a lossless DMA with a constant output inertia, if internal dissipation is neglected ($T_v = T_c = 0$), (27) reduces to

$$M \begin{bmatrix} \ddot{\theta}_S \\ \ddot{\theta}_R \end{bmatrix} + R_{SR} T_L = \mathbf{0} \quad \Rightarrow \quad \begin{bmatrix} \ddot{\theta}_S \\ \ddot{\theta}_R \end{bmatrix} = -M^{-1} R_{SR} T_L. \tag{28}$$

Using Eq. (1) derivatives, the output acceleration becomes

$$\ddot{\theta}_L = -u^\top M^{-1} u T_L, \tag{29}$$

with $u = [R_S \; R_R]^\top$. The DMA's output inertia is therefore

$$J_{\text{out}} = \left(u^\top M^{-1} u\right)^{-1}, \tag{30}$$

which depends only on the inertias (J_S, J_R, J_o) and gear factors (R_S, R_R) embedded in M and u.

For clarity, we define the actuator's impulsive reflected inertia as the scalar quantity that maps an instantaneous change in output velocity to the corresponding generalized momentum seen at the contact point. For the DMA in its dual-motor mode, this quantity reads

$$J_{\text{ref,act}}^{\text{DMA}} = J_o + \left(\frac{R_S^2}{J_S} + \frac{R_R^2}{J_R}\right)^{-1}, \tag{31}$$

which follows from the mass matrix M and the kinematic mapping $u = [R_S \; R_R]^\top$. When one of the drive trains is locked, the reflected actuator inertia reduces to

$$J_{\text{ref,act}}^{\text{sun locked}} = J_o + \frac{J_R}{R_R^2}, \tag{32}$$

$$J_{\text{ref,act}}^{\text{ring locked}} = J_o + \frac{J_S}{R_S^2}, \tag{33}$$

corresponding to single-drive operation through the remaining free motor.

Crucially, J_{out} is independent of the internal speed distribution γ meaning that in a lossless, passive DMA the environment perceives a constant inertia regardless of how kinetic energy is shared between the two motors.

The robot's effective collision mass is thus

$$m_r^{\text{DMA}} = M_{\text{pl}} + \frac{J_L + J_{\text{out}}}{l^2}, \tag{34}$$

and the coupled robot-human system reduces to the same scalar form used for the SDA,

$$m_{\text{eff}}^{\text{DMA}} \ddot{x} + c_{\text{eff}} \dot{x} + k_{\text{eff}} x = m_{\text{eff}}^{\text{DMA}} g, \tag{35}$$

with $m_{\text{eff}}^{\text{DMA}} = m_r^{\text{DMA}} + m_h$. Since $m_{\text{eff}}^{\text{DMA}}$ does not depend on γ, the closed-form expressions of Appendix A predict identical $F_{\max}$ and $t_{\max}$ for all γ. This matches the lossless simulations, which show that different internal speed ratios yield the same peak force when internal friction is absent.

In a DMA with viscous and Coulomb friction

$$T_v = \begin{bmatrix} \nu_S \dot{\theta}_S \\ \nu_R \dot{\theta}_R \end{bmatrix}, \qquad T_c = \begin{bmatrix} \text{sign}(\dot{\theta}_S) T_{cS} \\ \text{sign}(\dot{\theta}_R) T_{cR} \end{bmatrix}, \qquad \dot{\theta}_S \approx \frac{(1-\gamma_0)\dot{\theta}_L}{R_S}, \qquad \dot{\theta}_R \approx \frac{\gamma_0 \dot{\theta}_L}{R_R}.$$

The output torque due to viscous friction is

$$T_{v,L} \approx (\nu_S (1-\gamma_0) + \nu_R \gamma_0) \dot{\theta}_L,$$

which maps to a contact-space damping

$$c_{\text{act}}(\gamma_0) = \frac{\nu_S (1-\gamma_0) + \nu_R \gamma_0}{l^2}. \tag{36}$$

Thus the total effective damping becomes

$$c_{\text{tot}}(\gamma_0) = c_{\text{eff}} + c_{\text{act}}(\gamma_0), \tag{37}$$

giving the DMA a γ-dependent dissipation profile.

In the case of Coulomb friction, it yields an output force

$$F_{c,\text{act}} = \frac{R_S T_{cS} + R_R T_{cR}}{l} \, \text{sign}(\dot{x}), \tag{38}$$

which is approximately independent of γ_0 during the first half-cycle. Including both friction terms, the DMA collision dynamics become

$$m_{\text{eff}}^{\text{DMA}} \ddot{x} + c_{\text{tot}}(\gamma_0) \dot{x} + k_{\text{eff}} x + F_{c,\text{act}} \text{sign}(\dot{x}) = m_{\text{eff}}^{\text{DMA}} g. \tag{39}$$

Neglecting Coulomb friction in closed form, the Appendix A solution applies by replacing $c_{\text{eff}} = c_{\text{tot}}(\gamma_0)$, yielding γ-dependent natural frequency, damping ratio, and peak force. Coulomb friction can be included using an equivalent viscous approximation or an energy-balance correction for the first peak.

Simulating Eq. (39) with $\dot{x}_{mr}(0) = 0.5$ m/s and $\gamma_0 \in [0, 1]$ produces peak forces ranging from 358 N to 383 N, with a minimum around $\gamma_0 \approx 0.25$ as depicted in Fig. 11. Compared to the SDA results presented in Section 3.1.2, the DMA reduces the peak collision force by 11% relative to the low inertia SDA configuration (decreasing from 402 N to 358 N), and by 46% compared to the high inertia SDA configuration (decreasing from 665 N to 358 N). These results highlight the capability of the DMA to passively regulate collision severity through its lower overall kinetic energy.

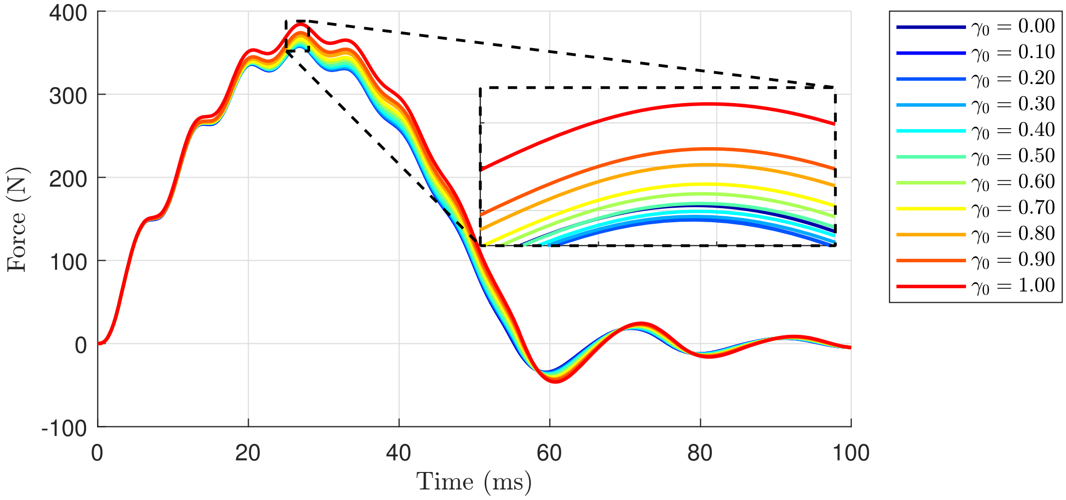

Fig. 11. Collision response of the DMA across different initial speed distributions γ_0. Peak forces are close to each other regardless of γ_0, ranging from 358 to 383 N. Small deviation depends on the friction parameter of each drive train, while in a non-friction situation, all forces are similar.

4. Experimental evaluation

To experimentally evaluate the collision response of the proposed actuation strategies, a test setup was built around a DMA configuration with the design parameters summarized in Table 1, and the schematic shown in Fig. 1 and the hardware implementation illustrated in Fig. 12. A rigid link is mechanically connected to the actuator's output and used to deliver controlled collisions to a compliant target surface. The impact target in all experiments is the PRMS (Pilz Robot Measurement System), a certified measurement device that complies with ISO/TS 15066 and is specifically designed to assess safety in human-robot interactions. This system includes interchangeable springs and silicone rubber layers that emulate the mechanical impedance of human body parts.

All experiments are performed with the PRMS sampling at a fixed rate of 2 kHz, ensuring high-fidelity force measurements. The robot executes predefined trajectories while varying actuator modes (e.g., single-drive or dual-drive configurations) to study their effect on collision dynamics. The goal of these experiments is to quantify the peak force transmitted during impact and analyze how actuation strategy and motor coordination influence collision safety.

To investigate collision dynamics without active control during impact, the robot follows the trajectory using a torque-controlled scheme that includes feedforward terms and gravity compensation. Immediately before contact, the commanded motor torques are set to zero, effectively disabling all control action and allowing the system to move freely after impact. The following trajectory depicted in Fig. 13 and its response during impact, illustrate this scenario.

To investigate the impact dynamics and the effectiveness of different actuation strategies in collision scenarios, three distinct experiments were conducted. These experiments aimed to evaluate collision detection speed, peak impact force, and the potential benefits of using a DMA compared to a traditional SDA.

A spring with a stiffness of 10 N/mm was used as the most compliant representation of human body interaction in these experiments. It is acknowledged that higher stiffness values result in significantly greater impact forces beyond the force sensor limit and it is unsafe.

4.1. Effect of sampling rate on collision detection and peak force response

This experiment investigates how the data acquisition sampling rate of sensor signals affects the speed and accuracy of collision detection and its subsequent influence on peak interaction forces. The primary objective is to determine how quickly a collision signal can be identified based on environment force estimation, using only motor current sensing and velocity feedback. In this experiment, there is also no control applied upon detecting a collision, as a zero-torque signal is fed to the motor.

In this experiment, to ensure consistency, the collision location and direction are fixed, and the properties of the collided surface and its stiffness are constant across all experiments. The robot executes a predefined motion trajectory, and three experimental trials are conducted with identical mechanical and control configurations, differing only in sampling rate: 1 ms (1 kHz), 2 ms (500 Hz), and 5 ms (200 Hz).

For each sampling condition, the environment force is estimated using a current-based observer and filtered motor velocity feedback. The estimation bandwidth and filter cutoff frequencies are tuned such that the force remains within ± 10 N during free motion, ensuring minimal signal lag while suppressing noise. A collision is detected when the estimated force crosses a threshold band of ± 15 N, as depicted by the dashed boundary lines in Fig. 14a.

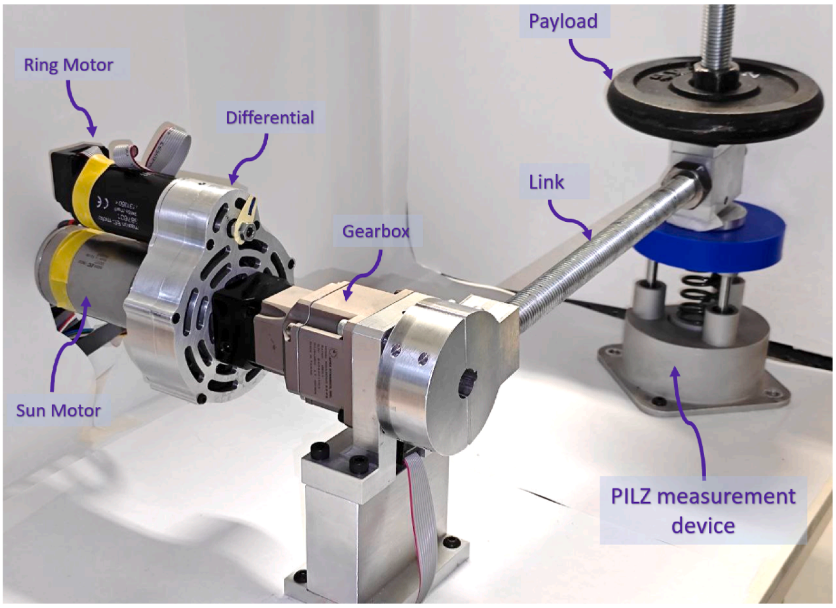

Fig. 12. Collision simulation setup. A DMA with the potential to convert an SDA is utilized to study collision behaviour. To ensure all experiments run on the same setup, either the ring or sun motor is locked at zero position in SDA mode, and in DMA mode, both motors operate together.

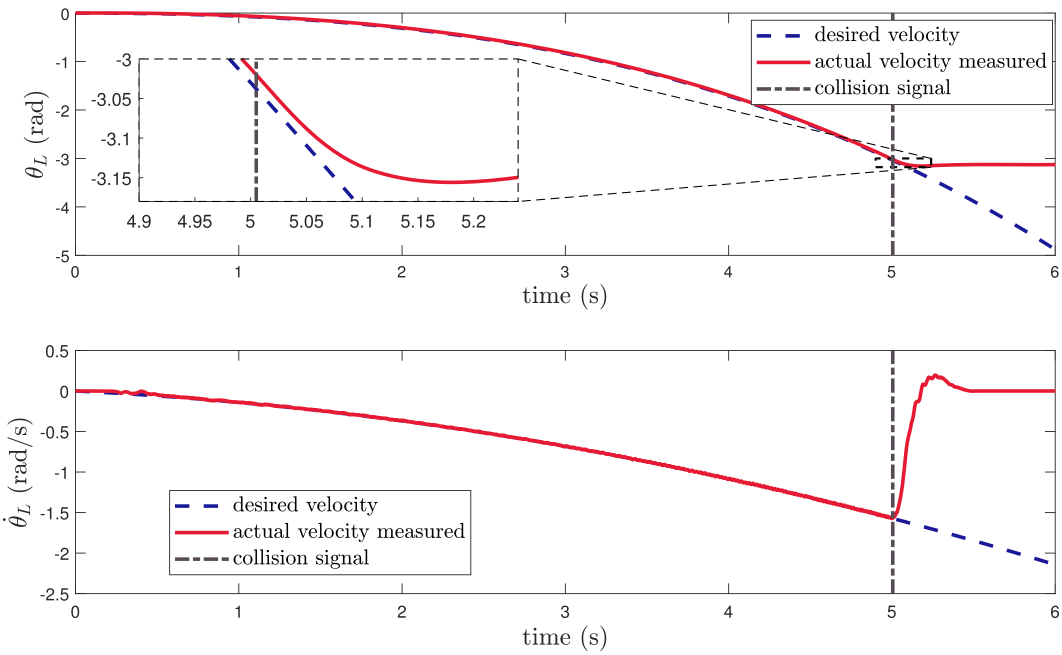

Fig. 13. Trajectory tracking before impact; actuator control signal set to zero right before impact. The vertical dashed line indicates the collision time. Since the controller does not play a role after the collision, this study investigates passive collision behavior to observe the pure interaction dynamics without any software control.

The results of Fig. 14a reveal that at a 1 ms sampling rate, the collision signal becomes positive after approximately 9 ms depicted in red. At 2 ms, detection is delayed to around 12 ms deptiched in green. At 5 ms, the collision signal is only triggered after approximately 30 ms depicted in blue, making real-time mitigation ineffective.

These delays directly affect the actuator's ability to react before peak force is reached. As illustrated in Fig. 14b, the peak collision forces under each condition were: 39 N at 1 kHz, 46 N at 500 Hz, and over 101 N at 200 Hz, where the response to identify impact was too slow at later case and more than 60% of peak force applied to environment upon positive collision signal. These results of real impact, which measured with PILZ setup at 2 kHz sampling rate highlight the critical role of high-frequency feedback in

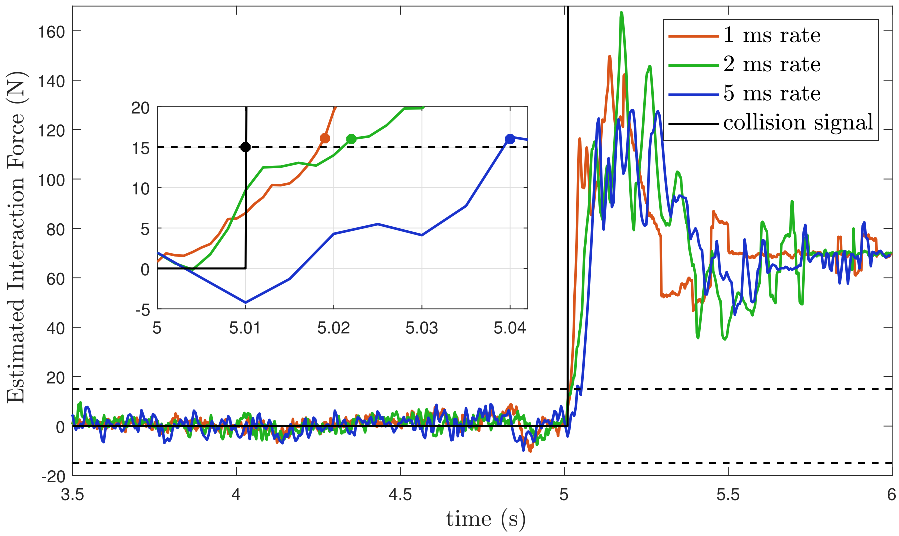

(a) Collision force estimation and collision identification at different sampling rates (1 ms = 1 kHz, 2 ms = 500 Hz, and 5 ms = 200 Hz). The dashed lines indicate the ±15 N detection thresholds. Colored dots show the instant when the estimated interaction force first crosses the threshold.

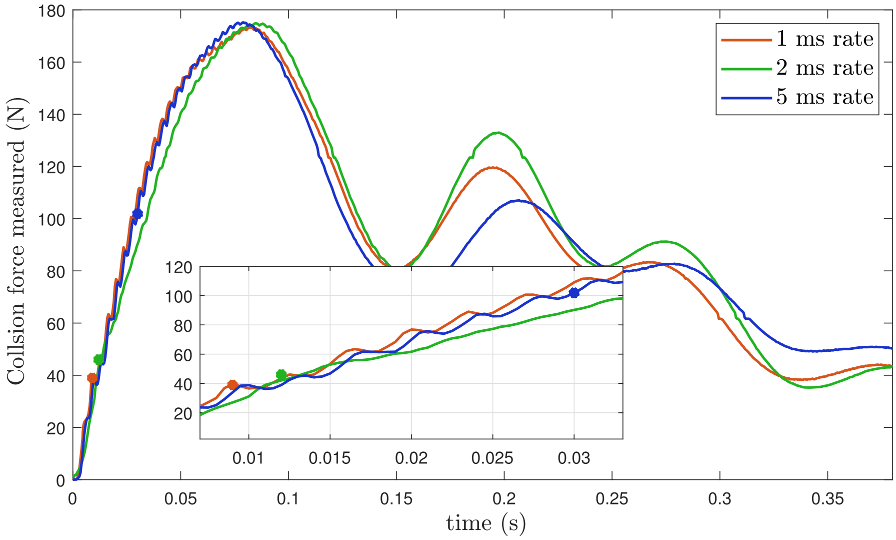

(b) PRMS-measured collision force at a 2 kHz sampling rate. The curves compare actuator control sampling rates of 1 ms, 2 ms, and 5 ms. The colored dots indicate detection moments: 39 N (1 kHz), 46 N (500 Hz), and over 101 N (200 Hz).

Fig. 14. Comparison of collision estimation and real measured interaction force for different controller sampling rates. These experiments highlight the importance of having the robot controller operate at or above 1 kHz. Higher sampling rates allow earlier detection and therefore reduce how much of the peak force has already occurred before the robot even realizes the collision happened. At 200 Hz, more than 60% of the peak force is already applied before detection.

collision-sensitive applications. Fast sampling not only improves the fidelity of force estimation, but the peak force estimation is also closer to reality. Also, the peak force estimated in the 5 ms sampling rate is hindered and is much less than the peak force we estimated in the 1 ms sampling rate. Also, a higher sampling rate creates a wider control window, allowing the possibility to reduce impact forces before they peak by applying control techniques like impedance control, which has been studied in [24].

It is important to clarify why active control was disabled in the collision experiments of this study. In our previous work [24], impedance control was applied during impact, and it was experimentally observed that DMA configurations exhibited lower peak forces than torque-equivalent SDAs, largely independent of the internal speed ratio. This raised a fundamental question: was the observed improvement primarily due to control action, or due to intrinsic mechanical properties of the DMA architecture?

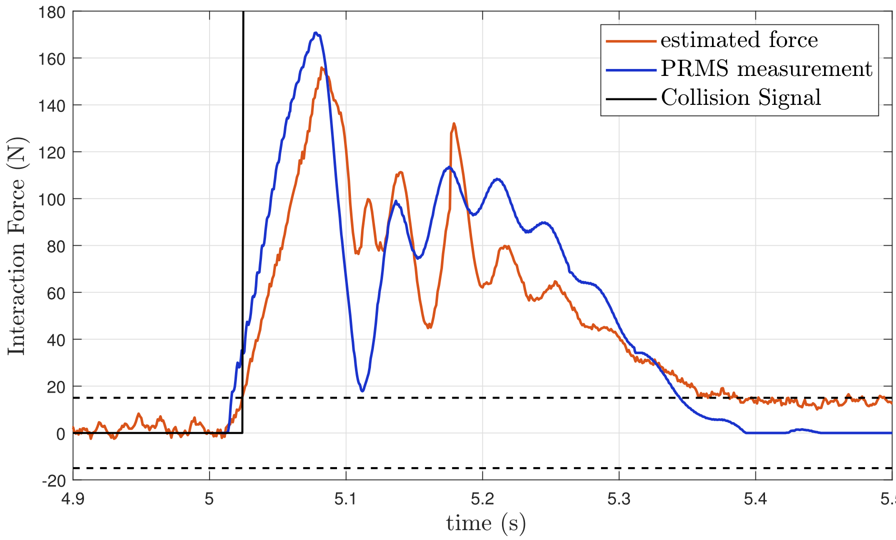

(a) Collision experiment with the sun motor tracking the trajectory and the ring motor locked at zero position. A peak interaction force of 170.7 N was recorded by the PRMS setup.

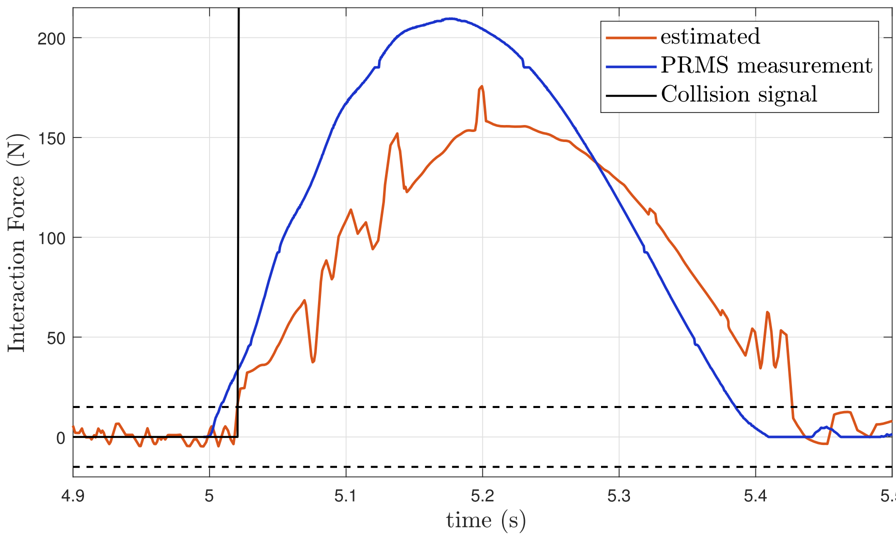

(b) Interaction force response when the ring motor is active and the sun motor is held at zero position. The peak force measured by the PRMS setup is 209 N, caused by the higher reflected inertia of the ring drivetrain.

Fig. 15. Comparison of collision responses for sun-motor actuation vs. ring-motor actuation in SDA mode. A bound of $\pm 15\,\mathrm{N}$ is used for collision signal detection. Similar to the simulations, the sun motor active (on the left) produces a lower peak force compared to the higher actuator inertia when the ring motor is active (on the right).

The results of the present sampling-rate study provide insight into this question. As shown, collision detection requires approximately 9 ms even at a 1 kHz sampling rate, while peak forces typically occur within 17-79 ms depending on system parameters. In many scenarios, a substantial portion of the peak force develops before any controller can react. This indicates that the initial collision phase is dominated by the system's passive mechanical properties, particularly reflected inertia and damping.

For this reason, control forces were deliberately disabled in this study to isolate the pure mechanical contribution of the actuator architecture. The results demonstrate that the DMA reduces peak forces even under purely passive conditions, confirming that its safety advantage originates from intrinsic inertia shaping rather than from active control intervention. While high-bandwidth control can further influence post-peak behavior, it has limited authority over the impulsive phase of uncontrolled collisions.

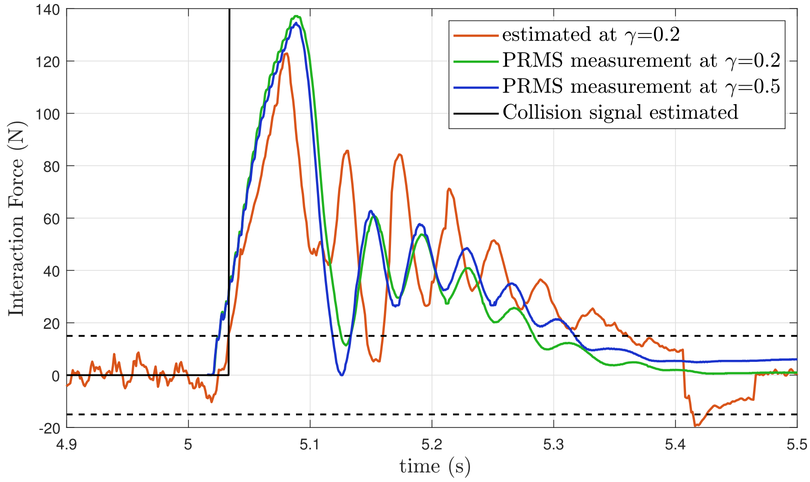

Fig. 16. Interaction force response in DMA mode with both motors active. Experiments were conducted for two different values of $\gamma = 0.2$ and 0.5. As observed in simulations, varying γ does not significantly affect the peak force. The measured peak force was 138 N, considerably lower than in the single-drive actuator cases, demonstrating the benefit of reduced reflected inertia in the DMA configuration. DMA operation reduces peak force by 19% relative to SDA-Sun and by 34% relative to SDA-Ring. Internal energy redistribution effectively lowers collision severity.

4.2. *DMA versus SDA in collision*

Following the insights gained from the previous sampling-rate study, all subsequent experiments were conducted with a 1 kHz sampling rate to ensure fast and reliable collision detection. Three experiments were performed to investigate the effect of actuation strategy on peak collision force in a DMA, considering its use as a single-drive actuator or with both motors contributing during collision. The goal was to study how activating different drivetrain configurations influences the impact response when tracking the same motion trajectory and colliding with a compliant surface measured via the PRMS setup.

In the first scenario, only the sun motor was commanded to track the trajectory while the ring motor was kept immobilized at a fixed position. This configuration mimics a single-drive actuator operating through the sun-side drivetrain. The result of this experiment is shown in Fig. 15a. The peak interaction force recorded by the PRMS setup reached 170.7 N. The oscillatory behavior following impact is due to the system dynamics and spring response of the PRMS surface. The corresponding real impact force upon identification of the collision, when the estimated collision force surpasses the upper bound, is 34 N.

In the second case, the ring motor was responsible for motion tracking, while the sun motor was held in place, so an SDA in a different configuration was tested. Since the ring drivetrain has a higher gear reduction and also higher reflected inertia, a higher peak force is expected. As depicted in Fig. 15b, the measured peak force increased to 209 N, confirming the dominant influence of drivetrain inertia on collision response.

In the third experiment, both sun and ring motors contributed to trajectory tracking under coordinated motion, enabling operation in full DMA mode. Two configurations were studied with different internal motor speed distributions: $\gamma = 0.2$ and $\gamma = 0.5$. The results are presented in Fig. 16. The maximum peak force recorded was approximately 138 N, which is considerably lower than the single-drive experiments. Moreover, the results show that varying γ does not lead to significant differences in peak force, consistent with simulation findings. The reduced reflected inertia and energy redistribution capability of the DMA architecture contribute to improved impact mitigation in these configurations.

These findings demonstrate that the DMA offers a significant improvement in collision safety by reducing the impact forces experienced during collision events. The experiments confirm that actuation strategy, sampling rate, and inertia play critical roles in determining the severity of an impact and the system's ability to mitigate it effectively.

5. Conclusion and future work

This study presented a comprehensive analysis of collision safety using Dual Motor Actuators (DMA) under uncontrolled impact conditions, supported by simulation, analytical modeling, and experimental validation. Simulation results demonstrate that the DMA can reduce peak collision forces by 11% to 46% compared to single drive actuator (SDA) configurations, depending on stiffness and payload conditions. Experimental results, conducted within the safe operating limits of the measurement setup, confirm peak force reductions of up to 34% relative to SDA configurations. These results show that the achievable reduction depends on collision conditions and system parameters. The mitigation capability arises from the DMA's ability to redistribute kinetic energy between two drive trains and its lower overall reflected inertia.

We also introduced a simplified analytical model that predicts peak force and response time with high accuracy across a wide range of scenarios, offering valuable insight for actuator design and safety-oriented control strategies.

Experiments were performed with single-drive configurations, where either the sun motor was active while the ring motor was locked, or the ring motor was active while the sun motor was locked. In both cases, collision responses were compared to coordinated dual motor actuators (DMAs). Furthermore, we demonstrated that high-frequency feedback (1 kHz) allows earlier collision detection after around 9 ms and a higher chance to reduce peak forces with control scenarios compared to slower sampling rates that can increase collision confirmation time to 30 ms for 200 Hz sampling rate. Although very soft and thick padding around the robot moving structures can also reduce impact forces, as discussed in Section 2.7, it comes with drawbacks. For example, covering a cylindrical robot link of 8 cm diameter and 40 cm length with a 15 mm soft silicone layer (density $= 1.1\ g/cm^3$) would add approximately 1650 g of mass. This additional mass not only increases the robot's energy consumption during motion but also raises the effective impact mass, directly counteracting safety improvements. In contrast, DMA achieves collision force reduction without adding significant passive mass, making it a more efficient and scalable solution for safety-critical robots.

Beyond safety, DMAs also offer other advantages reported in previous studies, such as improved efficiency and flexible energy distribution between drive trains [23,33], which can reduce overall energy consumption and enhance control versatility. Nevertheless, for safety applications specifically, their added complexity, controller demands, and drivetrain mass must still be carefully weighed against the gains. Future research should investigate whether one motor can remain passive or activate only during collisions to minimize energy loss and reduce hardware demands. It also remains open how best to deploy DMA in multi-DOF systems, where actuator mass and redundancy can significantly affect dynamics and subsequently safety concerns. The integration of intelligent control strategies, such as adaptive impedance or inertia shaping, into DMA could further enhance safety.

Declaration of generative AI and AI-assisted technologies in the writing process

During the preparation of this work the authors used GPT5 in order to improve language and readability, with caution. After using this tool/service, the authors reviewed and edited the content as needed and take full responsibility for the content of the publication.

CRediT authorship contribution statement

Amin Khorasani: Writing – review & editing, Writing – original draft, Visualization, Validation, Methodology, Investigation, Formal analysis, Data curation, Conceptualization; **Thierry Hubert:** Writing – review & editing, Formal analysis; **Nathan Desmedt:** Methodology; **Raphaël Furnémont:** Writing – review & editing, Supervision; **Alexandre Girard:** Writing – review & editing, Supervision, Methodology, Conceptualization; **Bram Vanderborght:** Writing – review & editing, Supervision; **Tom Verstraten:** Writing – review & editing, Supervision, Resources, Project administration, Methodology, Funding acquisition, Conceptualization.

Data availability

Data will be made available on request.

Declaration of competing interest

The authors declare that they have no known competing financial interests or personal relationships that could have appeared to influence the work reported in this paper.

Appendix A. Derivation of peak force and time-to-peak expressions

We derive here the closed-form expressions for the first maximum displacement and the corresponding peak collision force used in Section 2.6. The system dynamics are modeled as a mass-spring-damper under gravity:

$$m_{\text{eff}}\,\ddot{x}(t) + c_{\text{eff}}\,\dot{x}(t) + k_{\text{eff}}\,x(t) = m_{\text{eff}}\,g, \tag{A.1}$$

where m_{eff} is the effective mass, k_{eff} the effective stiffness, and c_{eff} the damping coefficient.

In case of collsion in direction with gravity, it shifts the static equilibrium position to

$$x_g = \frac{m_{\text{eff}}\,g}{k_{\text{eff}}}.$$

Defining the displacement relative to equilibrium,

$$y(t) = x(t) - x_g,$$

the dynamics become homogeneous:

$$m_{\text{eff}}\,\ddot{y}(t) + c_{\text{eff}}\,\dot{y}(t) + k_{\text{eff}}\,y(t) = 0. \tag{A.2}$$

The standard definitions apply:

$$\omega_n = \sqrt{\frac{k_{\text{eff}}}{m_{\text{eff}}}}, \qquad \zeta = \frac{c_{\text{eff}}}{2\sqrt{k_{\text{eff}} m_{\text{eff}}}}, \qquad \omega_d = \omega_n\sqrt{1-\zeta^2}. \tag{A.3}$$

For $0 < \zeta < 1$ (underdamped case), the response is

$$y(t) = Ae^{-\zeta\omega_n t}\cos(\omega_d t + \phi), \tag{A.4}$$

with constants A, ϕ from initial conditions. For an impact without pre-compression:

$$x(0) = 0, \quad \dot{x}(0) = v_0,$$

which yields

$$y(0) = -x_g, \quad \dot{y}(0) = v_0.$$

Thus

$$A = \sqrt{y(0)^2 + \left(\frac{v_0 + \zeta\omega_n y(0)}{\omega_d}\right)^2}, \tag{A.5}$$

$$\phi = \operatorname{atan2}\big(-v_0 - \zeta\omega_n y(0),\ \omega_d y(0)\big). \tag{A.6}$$

Differentiating $y(t)$ and setting $\dot{y}(t) = 0$ gives

$$\tan(\omega_d t + \phi) = -\frac{\zeta\omega_n}{\omega_d}. \tag{A.7}$$

The smallest positive solution corresponds to the first maximum:

$$t_{\max} = \frac{-\arctan\left(\frac{\zeta}{\sqrt{1-\zeta^2}}\right) - \phi + k\pi}{\omega_n\sqrt{1-\zeta^2}}. \tag{A.8}$$

Using the atan2 implementation ensures numerical robustness. The minimum k for the first selected positive peak time is normally 0 or 1. At $t_{\max}$, the cosine term evaluates to $\pm\sqrt{1-\zeta^2}$, leading to

$$x_{\max} = x_g + A\, e^{-\zeta\omega_n t_{\max}}\sqrt{1-\zeta^2}, \tag{A.9}$$

$$F_{\max} = k_{\text{eff}}\, x_{\max}. \tag{A.10}$$

These expressions provide closed-form estimates of the time-to-peak and peak collision force, depending only on the effective mass, stiffness, damping, and impact velocity. They form the analytical basis for comparison with physics-based simulations in Section 2.6.

References

[1] X. Yang, Z. Zhou, L. Li, X. Zhang, Collaborative robot dynamics with physical human–robot interaction and parameter identification with PINN, Mech. Mach. Theory 189 (2023) 105439.
[2] C. Scholz, H.-L. Cao, E. Imrith, N. Roshandel, H. Firouzipouyaei, A. Burkiewicz, M. Amighi, S. Menet, D.W. Sisavath, A. Paolillo, et al., Sensor-enabled safety systems for human-robot collaboration: a review, IEEE Sens. J. 25 (2024) 65–88.
[3] S. Haddadin, A. De Luca, A. Albu-Schäffer, Robot collisions: a survey on detection, isolation, and identification, IEEE Trans. Rob. 33 (6) (2017) 1292–1312.
[4] U.E. Ogenyi, J. Liu, C. Yang, Z. Ju, H. Liu, Physical human–robot collaboration: robotic systems, learning methods, collaborative strategies, sensors, and actuators, IEEE Trans. Cybern. 51 (4) (2019) 1888–1901.
[5] T. Hubert, A. Khorasani, M. Usman, H. Nouhi, R. Furnémont, B. Vanderborght, G. Van De Perre, T. Verstraten, Cobots designed for strength, not stiffness, IEEE Access 13 (2025) 129787–129802.
[6] T. Hubert, A. Khorasani, M. Usman, H. Nouhi, R. Furnémont, J. Lataire, B. Vanderborght, G. Van De Perre, T. Verstraten, Vibration control and performance analysis of a 3DOF high-payload flexible link manipulator, IEEE Access 13 (2025) 118547–118564.
[7] I. Görgülü, M.I.C. Dede, G. Kiper, A new safe flexible torsion joint design with softening stiffness characteristics, Mech. Mach. Theory 210 (2025) 106015.
[8] A. Calanca, P. Fiorini, A rationale for acceleration feedback in force control of series elastic actuators, IEEE Trans. Rob. 34 (1) (2018) 48–61.
[9] Z. Lyu, Y. Cao, M.Y. Wang, Q. Xu, Concept design of a monolithic compliant series-elastic actuator with integrated position and two-level force sensing, Mech. Mach. Theory 193 (2024) 105569.
[10] C. Schneider, M.M. Seizmeir, T. Suchanek, M. Hutter-Mironovová, M. Bdiwi, M. Putz, Empirical analysis of the impact of additional padding on the collaborative robot velocity behavior in transient contact cases, in: ICINCO, 2021, pp. 216–223.
[11] C. Fischer, M. Neuhold, M. Steiner, T. Haspl, M. Rathmair, S. Schlund, Collision tests in human-robot collaboration: experiments on the influence of additional impact parameters on safety, IEEE Access 11 (2023) 118395–118413.
[12] G. Pang, G. Yang, W. Heng, Z. Ye, X. Huang, H.-Y. Yang, Z. Pang, CoboSkin: soft robot skin with variable stiffness for safer human–robot collaboration, IEEE Trans. Ind. Electron. 68 (4) (2020) 3303–3314.
[13] F. Gosselin, F. Ferlay, A. Janot, Development of a new backdrivable actuator for haptic interfaces and collaborative robots, in: Actuators, vol. 5, MDPI, 2016, p. 17.
[14] P.L. Garcia, S. Crispel, A. Varadharajan, E. Saerens, T. Verstraten, B. Vanderborght, D. Lefeber, R2power: The proof-of-concept of a backdrivable, high-ratio gearbox for human-robot collaboration, in: 2022 International Conference on Robotics and Automation (ICRA), IEEE, 2022, pp. 01–07.
[15] F. Ostyn, B. Vanderborght, G. Crevecoeur, Series clutched actuation for collision-tolerant high-speed robots, J. Mech. Robot. 16 (12) (2024) 9.
[16] I. Lalonde, J. Denis, M. Lamy, A. Girard, A dual-motor actuator for ceiling lift with high-force and high-speed capabilities, in: Actuators, 14, MDPI, 2025, p. 92.
[17] T. Verstraten, R. Furnémont, P. López-García, D. Rodriguez-Cianca, H.-L. Cao, B. Vanderborght, D. Lefeber, Modeling and design of an energy-efficient dual-motor actuation unit with a planetary differential and holding brakes, Mechatronics 49 (2018) 134–148.
[18] J. Bell, H.H. Asada, Design and time-optimal control of a high-speed high-torque dual-motor actuator, in: 2020 American Control Conference (ACC), IEEE, 2020, pp. 1017–1024.
[19] A. Shu, C. Raschel, M. Keppler, A. Wedler, M. Görner, Impact robustness vs. torque bandwidth: a design guide for differential elastic actuators, IEEE Trans. Rob. 40 (2024) 3657–3675.
[20] R.-J. Wang, H.-P. Huang, ADEA-active variable stiffness differential elastic actuator: design and application for safe robotics, in: 2011 IEEE International Conference on Robotics and Biomimetics, IEEE, 2011, pp. 2768–2773.
[21] M. Lauria, M.-A. Legault, M.-A. Lavoie, F. Michaud, Differential elastic actuator for robotic interaction tasks, in: 2008 IEEE International Conference on Robotics and Automation, IEEE, 2008, pp. 3606–3611.

[22] S. Crispel, P.L. Garcia, A. Varadharajan, A. Khorasani, E. Saerens, D. Lefeber, T. Verstraten, The model and design of a spring-embedded planetary dual-motor actuator to reduce energy losses, Mech. Mach. Theory 190 (2023) 105442.
[23] T. Verstraten, R. Furnémont, P. Lopez-Garcia, D. Rodriguez-Cianca, B. Vanderborght, D. Lefeber, Kinematically redundant actuators, a solution for conflicting torque–speed requirements, Int. J. Rob. Res. 38 (5) (2019) 612–629.
[24] A. Khorasani, M. Usman, T. Hubert, R. Furnémont, D. Lefeber, B. Vanderborght, T. Verstraten, Mitigating collision forces and improving response performance in human-robot interaction by using dual-motor actuators, IEEE Rob. Autom. Lett. 9 (2024) 5982–5989.
[25] A. Khorasani, R. Furnémont, M. Usman, T. Hubert, B. Vanderborght, D. Lefeber, G. Van de Perre, T. Verstraten, A methodology for designing a lightweight and energy-efficient kinematically redundant actuator, IEEE Rob. Autom. Lett. 7 (4) (2022) 10786–10793.
[26] S. Haddadin, S. Haddadin, A. Khoury, T. Rokahr, S. Parusel, R. Burgkart, A. Bicchi, A. Albu-Schäffer, On making robots understand safety: embedding injury knowledge into control, Int. J. Rob. Res. 31 (13) (2012) 1578–1602.
[27] F. Ballen-Moreno, K. Langlois, P. Ferrentino, J. Brancart, C. Van Vlerken, B. Vanderborght, N. Buls, T. Verstraten, Robotically aided method to characterise the soft tissue interaction with wearable robots, in: 2023 International Conference on Rehabilitation Robotics (ICORR), IEEE, 2023, pp. 1–6.
[28] Y. She, S. Song, H.-J. Su, J. Wang, A comparative study on the effect of mechanical compliance for a safe physical human–robot interaction, J. Mech. Des. 142 (6) (2020) 063305.
[29] O. Khatib, Inertial properties in robotic manipulation: an object-level framework, Int. J. Rob. Res. 14 (1) (1995) 19–36.
[30] M. Hamad, N. Mansfeld, S. Abdolshah, S. Haddadin, The role of robot payload in the safety map framework, in: 2019 IEEE/RSJ International Conference on Intelligent Robots and Systems (IROS), IEEE, 2019, pp. 195–200.
[31] R.J. Kirschner, N. Mansfeld, G.G. Peña, S. Abdolshah, S. Haddadin, Notion on the correct use of the robot effective mass in the safety context and comments on ISO/TS 15066, in: 2021 IEEE International Conference on Intelligence and Safety for Robotics (ISR), IEEE, 2021, pp. 6–9.
[32] K. Langlois, E. Roels, G. Van De Velde, C. Espadinha, C. Van Vlerken, T. Verstraten, B. Vanderborght, D. Lefeber, Integration of 3D printed flexible pressure sensors into physical interfaces for wearable robots, Sensors 21 (6) (2021) 2157.
[33] T. Verstraten, C. Schumacher, R. Furnémont, A. Seyfarth, P. Beckerle, Redundancy in biology and robotics: potential of kinematic redundancy and its interplay with elasticity, J. Bionic. Eng. 17 (2020) 695–707.